



Structural stability under Xe-ion irradiation of TiZrNbTaV-based high-entropy alloy and nitride films

Ji Wang^a, Rui Shu^{b,*}, Anna Elsukova^b, Smita G. Rao^b, Jianlong Chai^c, Yabin Zhu^c, Cunfeng Yao^c, Per O.Å. Persson^b, Arnaud le Febvrier^b, Per Eklund^b

^a School of Physical Science and Technology, Ningbo University, Ningbo 315211, China

^b Thin Film Physics Division, Department of Physics, Chemistry, and Biology (IFM), Linköping University, Linköping 58183, Sweden

^c Institute of Modern Physics, Chinese Academy of Sciences, Lanzhou 730000, China



ARTICLE INFO

Keywords:

High-entropy alloy
Nitrides
Ions irradiation
Transmission electron microscopy

ABSTRACT

Refractory high-entropy protective coatings are of interest for nuclear fuel cladding applications due to their corrosion resistant properties and irradiation resistance at elevated temperature. Here, TiZrNbTaV metallic and (TiZrNbTaV)N films were deposited by magnetron co-sputtering. The metal elemental contents of both films were nearly equiatomic. These films were irradiated by Xe ions at room temperature and 500 °C, and examined by X-ray diffraction and transmission electron microscopy. The as-deposited (TiZrNbTaV)N film showed a single NaCl-type fcc phase and a pronounced columnar growth structure, which could remain intact after irradiation treatments. In contrast, the as-deposited TiZrNbTaV film exhibited an amorphous structure and formed a bcc phase structure after irradiation at 500 °C. The TiZrNbTaV film after irradiation at 500 °C composed of depth-dependent size of grains. This distribution of grain size is consistent with simulated displacement damage. The stable structure of (TiZrNbTaV)N film under high temperature irradiation indicates that these materials have potential for use as protective coatings for nuclear fuel claddings.

1. Introduction

Coating technology for protecting structural materials used in environments with extreme irradiation is a versatile means to improve component stability and reliability for the development of accident-tolerant fuel [1]. Many coatings studied for cladding application are based on refractory metals or ceramic (e.g., nitride and carbide) materials, associated with properties such as resistance to radiation, chemical and high-temperature stability, high thermal conductivity, and hardness. During the last two decades, a class of emerging bulk materials, refractory high-entropy materials including metal alloys and ceramics [2], has been found to exhibit high radiation resistance [3–5] compared to their single or binary counterparts, which is attributed to their compositional complexity and lattice distortion [6]. Their stability in corroding and oxidizing environments at high temperatures may also benefit the application of cladding coatings. However, reports on the irradiation resistant behavior of refractory high-entropy materials in the form of films are relatively few.

Single-phase solid solution body-centered cubic (bcc) phase is

typically formed for most of refractory high-entropy alloy films. In contrast, the refractory nitrides can readily form stable NaCl-type interstitial nitrides. Small interstitial elements promote the recombination of irradiation-produced interstitials and vacancies [7]. Investigations of irradiation resistance of refractory high-entropy nitride films have been reported for different irradiation conditions. For instance, no amorphous and secondary phases were detected in (TiZrHfNbV)N coating after irradiating under either 200-MeV heavy Xe ions [8] or 500-keV He ions [9] at room temperature. The mechanical hardness of (TiHfZrNbTa)N film was improved after Au ion irradiation. No helium bubbles were detected in the AlCrMoNbZr/(AlCrMoNbZr)N multilayer under 400 keV He ions up to a fluence of 8×10^{16} ions/cm² [10]. For application in nuclear fuel assemblies, it is also crucial for the investigated high-entropy materials to avoid containing elements (e.g., Hf and B) with high thermal neutron absorption cross section [11]. Therefore, based on our previous works on the TiZrNbTa-based films [12,13], the TiZrNbTaV system was selected for investigation in this study.

To explore new promising candidate materials to be the protective

* Corresponding author.

E-mail address: rui.shu@liu.se (R. Shu).

coatings for nuclear fuel claddings, the present work aims to understand the structural stability and differences between refractory high-entropy alloy films and the corresponding nitride films under different Xe-ion irradiation conditions. We synthesized near-equiautomatic TiZrNbTaV and (TiZrNbTaV)N films on Al₂O₃(0001) substrates using magnetron sputtering. The irradiation experiments for both films were conducted by 3 MeV-Xe ions to a fluence of 2×10^{15} ions/cm² at room temperature and 500 °C, respectively. Their microstructural evolution and response to different irradiation conditions were analyzed and compared by X-ray diffraction (XRD) and Transmission Electron Microscopy (TEM).

2. Materials and methods

TiZrNbTaV alloy and TiZrNbTaV nitride films were deposited on Al₂O₃(0001) by (reactive) magnetron sputtering in an ultrahigh vacuum chamber (base pressure $< 10^{-8}$ Pa). A detailed description of the deposition system can be found elsewhere [14]. The target power of a compound Ti₂₅Nb₂₅Zr₂₅Ta₂₅ target (manufactured by Plansee Composite Materials GmbH) and elemental V target were set at 150 and 100 W, respectively. For the TiZrNbTaV metallic film, the gas flow of Ar was kept at 80 sccm corresponding to a working pressure of 0.5 Pa (3.5 mTorr), and the substrates were at floating potential without intentional heating. In reactive sputtering for TiZrNbTaV nitride films, the total gas flow of the Ar/N₂ mixture (65 % Ar/35 % N₂) was kept at 80 sccm, corresponding to a total pressure of 0.5 Pa (3.6 mTorr), and a negative substrate bias of 100 V was applied during deposition. The substrate holder was maintained at 400 °C with a constant rotation of 15 rpm. Al₂O₃(0001) and Si(100) substrates with a size of 10 × 10 mm² were cleaned sequentially with acetone and ethanol in an ultrasonic bath for 10 min, and finally blow-dried with nitrogen gas. The deposition time was kept 30 min for the TiZrNbTaV metallic film and 60 min for the TiZrNbTaV nitride film. The films deposited on sapphire were used for irradiation experiments, whereas the film grown on silicon was employed for composition analysis and anneal treatments.

The elemental composition of the TiZrNbTaV metallic film was measured by energy-dispersive X-ray spectrometry (EDS, Oxford Instruments X-Max), and that of the TiZrNbTaV nitride film was determined using EDS and time-of-flight elastic recoil detection analysis (ToF-ERDA). The EDS analyses were calibrated by ZAF methods. ToF-ERDA measurements were performed using a 36 MeV ¹²⁷I⁸⁺ beam at 67.5° incidence relative to the surface normal and a 45° recoil angle [15]. The data were analyzed using the simulation code Potku [16]. The content of the light elements nitrogen and oxygen were determined from ToF-ERDA (underneath 10 nm far from the top surface), while the content of metals was determined by setting nitrogen content to the results from ToF-ERDA, and normalizing metal contents from EDS, due to the overlap between Ti and V and between Nb and Zr in ToF-ERDA coincidence mappings. X-ray diffraction (XRD) was carried out with a Bragg-Bretano geometry on a PANalytical X'Pert powder diffractometer with a Cu source ($\lambda_{K\alpha} = 1.5406$ Å) operated at 45 kV/40 mA. TEM characterization was conducted with FEI Tecnai G2 TF20 UT instrument with a field emission gun operated at 200 kV and a Linköping's monochromated, high-brightness, double-corrected FEI Titan³, operated at 300 kV.

Xe ions were employed to irradiate the coatings in this study since Xe is a typical fission product with a relatively high fission yield in nuclear fuel assemblies [17,18]. Moreover, the working temperature in the nuclear fuel assemblies is below 500 °C in most pressure water nuclear reactors. Hence, irradiation temperatures were chosen at room temperature (RT) and 500 °C in order to provide the fundamental material-level understanding needed for future application. The 3 MeV-Xe ion irradiation experiments were conducted for 2.5 h at RT and 500 °C under a vacuum pressure of 10^{-5} Pa in a terminal chamber of the 320 kV multi-discipline research platform for highly charged ions at the Institute of Modern Physics, Chinese Academy of Sciences. The displacement damage caused by the 3 MeV Xe ions to a fluence of 2×10^{15} ions/cm² as

a function of depth in TiZrNbTaV and (TiZrNbTaV)N is calculated by stopping range of ions in matter (SRIM) codes with Kinchin-Pease quick-calculation mode, as shown in Fig. 1. The threshold energies were taken as the default values in the SRIM code as 25 eV for Ti, Zr, Nb, Ta, V and 28 eV for N, respectively. The densities were 8.4 g/cm³ for TiZrNbTaV and 8.6 g/cm³ for (TiZrNbTaV)N, respectively. The density of the nitride film was calculated based on the composition and the densities of their binary nitride counterparts [19]. Cross-sectional TEM specimens of these films irradiated at different temperatures were prepared by mechanically polishing down to 50 μm thickness, followed by Ar⁺-ion milling with a Gatan precision ion polishing system. Initially, the incident angle and energy of the Ar⁺ ions were set at 5° and 4.0 keV, respectively. During the final step, the energy value was decreased to 2.5 keV.

3. Results and discussion

The chemical composition of the TiZrNbTaV metallic and (TiZrNbTaV)N nitride films are displayed in atomic percent (at.%) in Table 1. The metal-element contents of the TiZrNbTaV metallic and (TiZrNbTaV)N films are both nearly equiautomatic within 2.0 % deviation. The nitrogen content of (TiZrNbTaV)N film is 51.0 %, indicating this film is a stoichiometric nitride, within the error margins (4.7 %, estimated according to the uncertainty propagation rule).

Fig. 2a shows XRD diffractograms of the as-deposited TiZrNbTaV film and the TiZrNbTaV film irradiated at RT and 500 °C. The as-deposited TiZrNbTaV film shows a sizeable broad peak centered at 37.6°, implying a fine-grained or amorphous structure. The intensity of this peak slightly decreases after irradiation at RT, and no distinct peak shift is found for both films after irradiation at different temperatures. However, for the TiZrNbTaV film irradiated at 500 °C, the intensity of the peak near ~37.6° becomes strong, and two additional peaks show up. These three peaks can be indexed to a single-phase body-centered cubic (bcc) phase. Meanwhile, the full width at half maximum (FWHM) of the (110) peak for the high temperature-irradiated film decreases, indicating the occurrence of grain coarsening. In contrast, the as-deposited and irradiated (TiZrNbTaV)N films all exhibit a 111-textured NaCl-type crystal structure, as shown in Fig. 2b. The (111) peak intensities for the (TiZrNbTaV)N films irradiated at RT and 500 °C are higher than the as deposited one, which means the crystallinities of these films were slightly improved after irradiation. At the same time, the right shift of the (111) peak implies a decrease in lattice constant

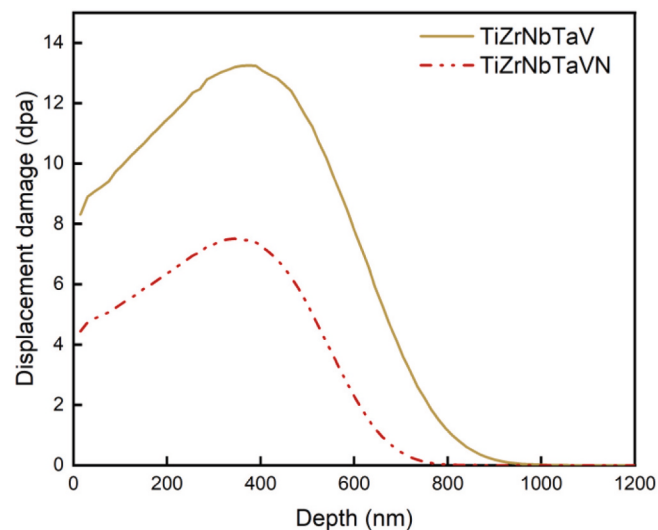


Fig. 1. Depth profiles of displacement per atom (dpa) predicted by SRIM code for the TiZrNbTaV metallic and (TiZrNbTaV)N films irradiated with 3-MeV Xe²⁰⁺ ions to a fluence of 2×10^{15} ions/cm².

Table 1

Chemical composition of the TiZrNbTaV metallic and (TiZrNbTaV)N nitride films estimated from a combination of ToF-ERDA and EDS.

Film	Thickness (nm)	Elemental composition (at.%)					
		Ti	Zr	Nb	Ta	V	N
TiZrNbTaV	560	21.0	18.9	18.8	20.6	20.7	0.0
TiZrNbTaVN	400	9.9	9.2	9.3	9.9	10.6	51.0

caused by irradiation both at RT and 500 °C. In comparison with the evolution of TiZrNbTaV films, less distinct change of crystallinity and grain coarsening are observed in (TiZrNbTaV)N film irradiated at 500 °C, which proves the crystal structure of (TiZrNbTaV)N film is more stable than its corresponding metallic film after irradiation at 500 °C.

The microstructure evolution of these metallic and nitride films after Xe-ion irradiation at RT was further investigated by TEM. Fig. 3a shows an overview image of the structure for the TiZrNbTaV metallic film with a thickness of ~560 nm. No observable crystalline feature is found in this uniform-contrast image. The selected area electron diffraction (SAED) pattern (Fig. 3b) shows a set of prominent amorphous rings. For the (TiZrNbTaV)N nitride film irradiated at RT, a distinct columnar structure is seen in the film with thickness of ~400 nm (Fig. 3c). The SAED pattern in Fig. 3d consists of ordered diffracted spots of a NaCl-type fcc phase and shows a (111) preferred orientation along the growth direction. Hence, the crystallinity of the (TiZrNbTaV)N nitride film could remain under RT irradiation conditions.

Fig. 4 shows the microstructural characterization of the TiZrNbTaV metallic and (TiZrNbTaV)N films after Xe-ion irradiation at 500 °C. These post-irradiation examinations were conducted using high-angle annular dark-field scanning transmission electron microscopy (HAADF-STEM) mode. The cross-sectional image of the TiZrNbTaV metallic film shows a distinctly different microstructure feature compared to the one irradiated at RT. In Fig. 4a, it can be seen that the grains near the surface are much smaller than grains near the Al₂O₃ substrate, which is further confirmed by the SAED patterns (Fig. 4b and c) acquired from the circled area near film surface and substrate, respectively. It shows more continuous and smaller-size spots in Fig. 4b than the spots found in Fig. 4c. Both sets of observed diffraction spots in Fig. 4b and c can be assigned to a bcc phase. No evidence of an amorphous phase is observed. Fig. 4d shows a region near the surface composed of equiaxed grains with a diameter ranging from 5 to 10 nm, while the grain size is above 50 nm near the substrate (Fig. 4e). Unlike the TiZrNbTaV metallic film, the general microstructure of (TiZrNbTaV)N nitride film irradiated at 500 °C, in Fig. 4f, shows typical columnar

features. The SAED patterns, obtained from the area near the surface (Fig. 4g) and close to the substrate (Fig. 4h), remain the same corresponding to an fcc phase. These results indicate a columnar structure with a high degree of crystallinity in both the top and bottom regions (Fig. 4i and j). The crystallinity of the nitride film after irradiation at 500 °C remains similar to the nitride irradiated at RT and shows less depth dependence than that of the metallic film.

The depth-dependent size of grains in TiZrNbTaV film observed after irradiation at 500 °C (Fig. 4a) may be influenced by two factors, i.e., annealing and irradiation. To further investigate which one is the dominant factor, the TiZrNbTaV film was annealed at 500 °C for 2.5 h (vacuum pressure <10⁻⁵ Pa). On the one hand, annealing may promote

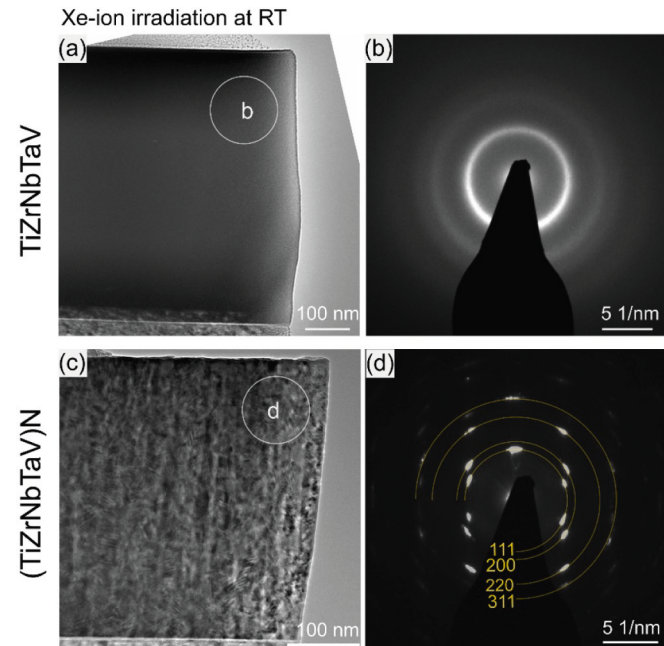


Fig. 3. Comparison of microstructural evolution along the growth direction between TiZrNbTaV metallic and (TiZrNbTaV)N nitride films under Xe-ion irradiation at RT. (a) Overview BFTEM image for TiZrNbTaV metallic film, (b) SAED pattern acquired from the circled area in a. (c) Overview BFTEM image for (TiZrNbTaV)N film, (d) SAED pattern acquired from the circled area in c.

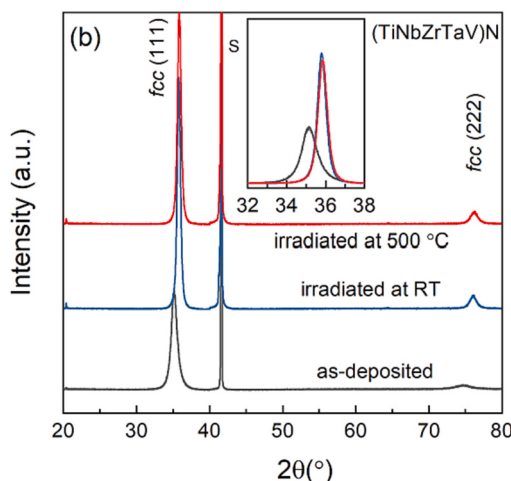
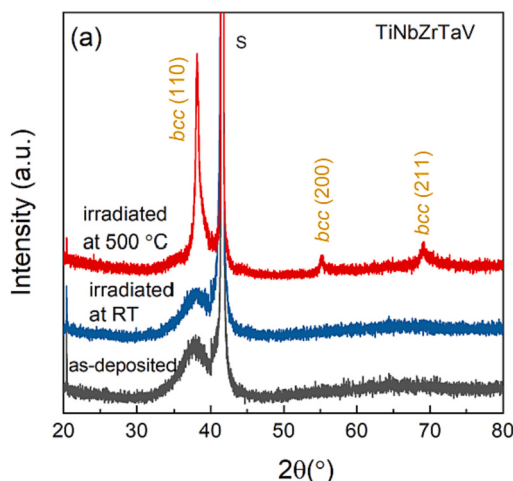


Fig. 2. (a) 0-2θ X-ray diffractograms of the TiZrNbTaV film on c-sapphire substrates in as-deposited state and after irradiated at RT, and 500 °C, respectively. (b) 0-2θ X-ray diffractograms of the (TiZrNbTaV)N films on c-sapphire substrates, before and after irradiated at RT, and 500 °C, respectively. Inset shows a zoomed 2θ-range from 30 to 38°.

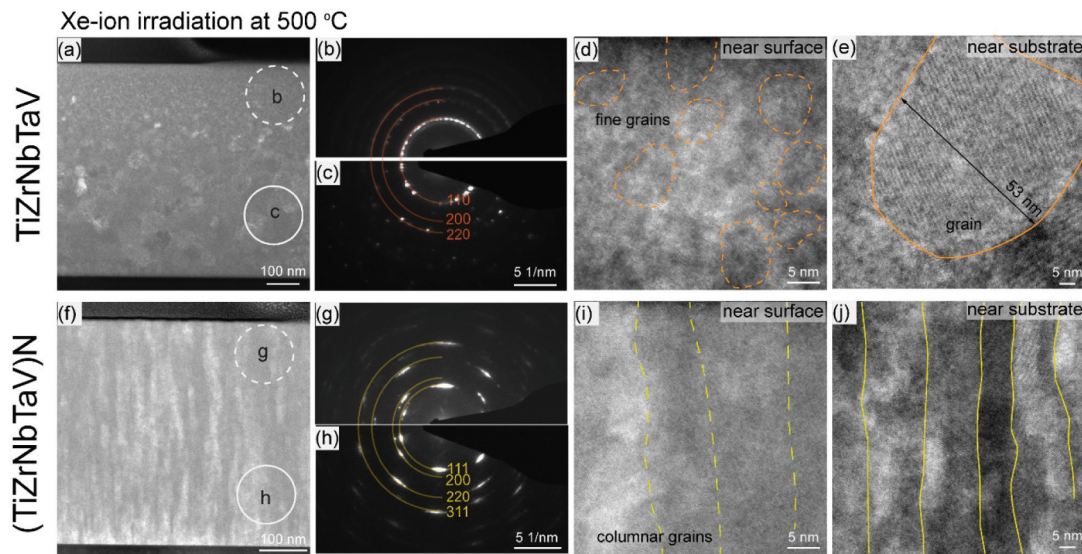


Fig. 4. Comparison of microstructural evolution between TiZrNbTaV metallic and (TiZrNbTaV)N films under Xe ions irradiation at 500 °C. (a) Overview HAADF-STEM image for metallic film. (b) and (c) SAED patterns acquired near the surface and substrate areas (labeled as the dash and solid circles in (a), respectively). (d) and (e) High-resolution STEM images near surface and substrate, respectively. (f) Overview HAADF-STEM image for the nitride film. (g) and (h) SAED patterns acquired near the surface and substrate areas (labeled as the dash and solid circles in (f), respectively). (i) and (j) High-resolution STEM images acquired near surface and substrate, respectively.

nucleation, grain growth, and even recrystallization due to defect annihilation and crystal recovery, which were proved by the fact that the annealed TiZrNbTaV film presents a weak 110 peak superimposed with a broad amorphous halo (Fig. SI1). In the refractory multicomponent systems TaNbHfZr [20], TiZrNbTaV [21], and TiZrNbTaHf [22,23], a similar change from an amorphous phase to crystalline bcc phases was found when increasing growth temperature from RT to high temperature (≥ 400 °C). Therefore, thermal-induced nucleation and homogenous bcc-phase-structure grain growth are reasonable to expect in this TiZrNbTaV film after annealing. However, the temperature is not the dominant reason causing the formation of depth-dependent size of grains, since no such a depth-dependent phenomenon was observed for the annealed TiZrNbTaV sample (Fig. SI2, TEM image and SAED pattern). Therefore, the other factor, irradiation effect, should be taken into consideration to explain the abnormal growth of grains. In this study, the (110) grains are pronouncedly observed in dark-field mode, and their sizes vary from a few to 55 nm in irradiation direction (Fig. 5). The distribution of grain size matches well with the Xe-ions induced displacement damage. Actually, irradiation induced grain growth was also reported in other literatures, e.g., Pt and Au films irradiated by Ar ions [24], ZrO₂ film irradiated by Au ions [25], NiFeCoCrCu nanocrystalline HEAs irradiated by Ni and Au ions [26]. However, grain size evolution along the ions penetration depth as shown in this study was seldom reported. As it has been well studied, loss of energetic ions in solid matters can be divided into two ways, i.e., energy of ions transferred to the lattice by electronic excitation (inelastic thermal spikes) [27,28] and by collisions among atomic nuclei (elastic thermal spikes) [29]. The former process is prominent during the initial stage of incident ions, especially when the ions have a high velocity. And the latter process dominates when the energetic ions slow down. The displacement damage of target materials (as calculated by SRIM code) are mainly caused by atomic nuclei collisions [30], therefore, this special grain size distribution hints that the elastic thermal spike produced by ions collision-induced cascades process dominates the grain growth process, which agrees with the previous studies [31–33]. Moreover, grain growth of TiZrNbTaV metallic film under Xe ion irradiation could occur above a specific temperature. These thermal energies trigger nucleation and assist the coarsening by favoring diffusion of irradiation-induced defects [34]. Therefore, nucleation and grain growth were not observed for the

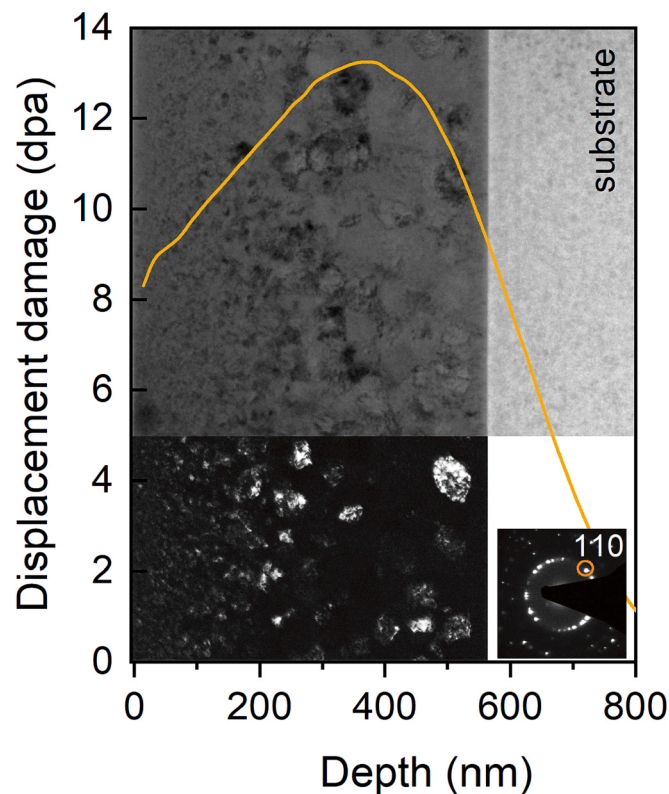


Fig. 5. Low-magnification BFTEM overviewing the grain size evolution for the TiZrNbTaV film irradiated at 500 °C, and (110) grains distribute in a dark-field TEM image obtained by the SAED pattern (near substrate). The red curve represents the depth distribution of displacement damage caused by 3-MeV Xe ions to a fluence of 2×10^{15} ions/cm².

TiZrNbTaV film irradiated at RT. Once the crystals form above a critical temperature, coarsening can be achieved due to a synergistic effect of thermal annealing and irradiation. The depth-dependence distribution

of grain size is a consequence of irradiation-induced displacement related phenomenon.

The good irradiation resistance of (TiZrNbTaV)N film originates from its intrinsic chemical properties and the special distribution of constituent atoms. Based on the previous investigations by Trachenko et al. [35,36], the long-range high ionicity of chemical bonding results in a relatively good amorphization resistance under irradiation conditions. The nature of ionic metal-nitrogen bondings in (TiZrNbTaV)N film therefore partly contributes to the resistance to amorphization during irradiation. Moreover, the preferential chemical affinity between nitrogen and specific metal constituents [37,38] results in a significant atomic-level compositional heterogeneity with increased lattice distortion and a rough atomic-level energy landscape [7]. During the dynamic process of energetic ions bombardment on target materials, a series of cascades are created until the energy of ions is lower than the threshold energy of lattice atoms to be displaced, and the corresponding energy of incident ions dissipates in the form of phonon scattering [39]. Subsequently, the rugged energy landscapes decrease the energy dissipation rate by increasing the phonon scattering [39,40], and prolong the energetic ions collision-induced thermal spike which promotes the annihilation of displaced atoms with vacancies [6], and finally improves the irradiation resistance. Similar irradiation-resistance enhancement by interstitial atoms has been also reported in FeMnCoCr-system by adding a small amount of carbon or nitrogen elements [7,41].

4. Conclusions

In summary, the near-equiautomatic refractory TiZrNbTaV metallic and nitride films were synthesized on Al₂O₃(0001) substrates using magnetron sputtering. The nitrogen content of as-deposited (TiZrNbTaV)N film was 51 at.% near stoichiometric. Both films were irradiated by 3 MeV-Xe ions to a fluence of 2×10^{15} ions/cm² at room temperature and 500 °C. The XRD results showed that the as-deposited TiZrNbTaV nitride film showed a single NaCl-type fcc phase in columnar growth structure, which could remain stable after irradiation at RT and 500 °C. The as-deposited TiZrNbTaV exhibited an amorphous structure and became a bcc phase structure after irradiation at 500 °C. Depth-dependence sizes of grains were found in the TiZrNbTaV film after irradiation at 500 °C, i.e., equiaxed grains with a diameter <10 nm near the surface, and coarsening grains above 50 nm near the substrate. Both thermal-induced and irradiation-induced grain growth played roles in this specific grain-size distribution.

CRediT authorship contribution statement

J. W. and R. S. initiated the study. P. E. and A. I. F. supervised the research. R. S. and S. G. R. synthesized samples with contributions from A. I. F. R. S. performed XRD measurements. J. W., J. C., Y. Z., and C. Y. performed the irradiation experiments. J. W., and R. S. prepared TEM specimens. A. E., R. S. performed the (S)TEM analysis with contributions from P. O. Å. P., J. W. and R. S. wrote the manuscript. All co-authors read, edited, and commented on successive version of the manuscript.

Declaration of competing interest

The authors declare no competing interests.

Data availability

The data that support these findings are available from the corresponding author on request.

Acknowledgements

The work was supported financially by the VINNOVA Competence Centre FunMat-II (grant no. 2016-05156), the Swedish Government

Strategic Research Area in Materials Science on Functional Materials at Linköping University (Faculty Grant SFO-Mat-LU No. 2009 00971), the Knut and Alice Wallenberg Foundation through the Wallenberg Academy Fellows program (KAW-2020.0196), the Swedish Research Council (VR) under project number 2021-03826, Natural Science Foundation of Zhejiang Province (No. LQ20A050001), Natural Science Foundation of Ningbo City (No. 2019A610183), and the State Key Laboratory of Digital Home Appliances (Hai er) No. KLDH202102. The Swedish Research Council and the Swedish Foundation for Strategic Research is acknowledged for access to ARTEMI, the Swedish National Infrastructure in Advanced Electron Microscopy through Grants No. 2021-00171 and RIF21-0026. Support from the Swedish Research Council VR-RFI (#2017-00646_9) for the Accelerator based ion-technological center, and from the Swedish Foundation for Strategic Research (contract RIF14-0053) for the tandem accelerator laboratory in Uppsala is gratefully acknowledged.

Appendix A. Supplementary data

Supplementary data to this article can be found online at <https://doi.org/10.1016/j.surcoa.2022.129198>.

References

- [1] S.J. Zinkle, K.A. Terrani, J.C. Gehin, L.J. Ott, L.L. Snead, Accident tolerant fuels for LWRs: a perspective, *J. Nucl. Mater.* 448 (2014) 374–379, <https://doi.org/10.1016/j.jnucmat.2013.12.005>.
- [2] A. Ostovari Moghadam, A. Cabot, E.A. Trofimov, Does the pathway for development of next generation nuclear materials straightly go through high-entropy materials? *Int. J. Refract. Met. Hard Mater.* 97 (2021), 105504 doi:10/gmxsb.
- [3] F. Wang, X. Yan, T. Wang, Y. Wu, L. Shao, M. Nastasi, Y. Lu, B. Cui, Irradiation damage in (Zr_{0.25}Ta_{0.25}Nb_{0.25}Ti_{0.25})C high-entropy carbide ceramics, *Acta Mater.* 195 (2020) 739–749, <https://doi.org/10.1016/j.actamat.2020.06.011>.
- [4] N. Jia, Y. Li, H. Huang, S. Chen, D. Li, Y. Dou, X. He, W. Yang, Y. Xue, K. Jin, Helium bubble formation in refractory single-phase concentrated solid solution alloys under MeV He ion irradiation, *J. Nucl. Mater.* 550 (2021), 152937, <https://doi.org/10.1016/j.jnucmat.2021.152937>.
- [5] G. Ge, F. Chen, X. Tang, Y. Wang, C. Li, Irradiation damage versus lattice distortion in AlNbTiVCr_x (x = 0, 0.5, 1) high-entropy alloys from first-principles calculations and irradiation experiments, *J. Nucl. Mater.* 563 (2022), 153630, <https://doi.org/10.1016/j.jnucmat.2022.153630>.
- [6] Y. Zhang, G.M. Stocks, K. Jin, C. Lu, H. Bei, B.C. Sales, L. Wang, L.K. Béland, R. E. Stoller, G.D. Samolyuk, M. Caro, A. Caro, W.J. Weber, Influence of chemical disorder on energy dissipation and defect evolution in concentrated solid solution alloys, *Nat. Commun.* 6 (2015) 8736, <https://doi.org/10.1038/ncomms9736>.
- [7] Z. Su, J. Ding, M. Song, L. Jiang, T. Shi, Z. Li, S. Wang, F. Gao, D. Yun, C. Lu, E. Ma, Radiation-tolerant high-entropy alloys via interstitial-solute-induced chemical heterogeneities, *ArXiv Prepr. ArXiv*, 2021. <http://arxiv.org/abs/2103.15134>. (Accessed 6 September 2021).
- [8] A.D. Pogrebnyak, A.A. Bagdasaryan, P. Horodek, V. Tarelny, V.V. Buranich, H. Amekura, N. Okubo, N. Ishikawa, V.M. Beresnev, Positron annihilation studies of defect structure of (TiZrHfNb)N nitride coatings under Xe¹⁴⁺ 200 MeV ion irradiation, *Mater. Lett.* 303 (2021), 130548 doi:10/gmpszt.
- [9] F.F. Komarov, A.D. Pogrebnyak, S.V. Konstantinov, Radiation resistance of high-entropy nanostructured (Ti,Hf,Zr,V,Nb)N coatings, *Tech. Phys.* 60 (2015) 1519–1524, <https://doi.org/10.1134/S1063784215100187>.
- [10] W. Zhang, M. Wang, L. Wang, C.H. Liu, H. Chang, J.J. Yang, J.L. Liao, Y.Y. Yang, N. Liu, Interface stability, mechanical and corrosion properties of AlCrMoNbZr/(AlCrMoNbZr)N high-entropy alloy multilayer coatings under helium ion irradiation, *Appl. Surf. Sci.* 485 (2019) 108–118, doi:10/gfz2v8.
- [11] V.F. Sears, Neutron scattering lengths and cross sections, *Neutron News* 3 (1992) 26–37, <https://doi.org/10.1080/10448639208218770>.
- [12] R. Shu, E.-M. Paschalidou, S.G. Rao, J. Lu, G. Grezynski, E. Lewin, L. Nyholm, A. le Febvrier, P. Eklund, Microstructure and mechanical, electrical, and electrochemical properties of sputter-deposited multicomponent (TiNbZrTa)N_x coatings, *Surf. Coat. Technol.* 389 (2020), <https://doi.org/10.1016/j.surcoa.2020.125651>.
- [13] J. Wang, R. Shu, J. Chai, S.G. Rao, A. le Febvrier, H. Wu, Y. Zhu, C. Yao, L. Luo, W. Li, P. Gao, P. Eklund, Xe-ion-irradiation-induced structural transitions and elemental diffusion in high-entropy alloy and nitride thin-film multilayers, *Mater. Des.* 219 (2022), 110749, <https://doi.org/10.1016/j.matdes.2022.110749>.
- [14] A. le Febvrier, L. Landälv, T. Liersch, D. Sandmark, P. Sandström, P. Eklund, An upgraded ultra-high vacuum magnetron-sputtering system for high-versatility and software-controlled deposition, *Vacuum*. 187 (2021), 110137, <https://doi.org/10.1016/j.vacuum.2021.110137>.
- [15] M.V. Moro, R. Holenák, L. Zendejas Medina, U. Jansson, D. Primetzhofer, Accurate high-resolution depth profiling of magnetron sputtered transition metal alloy films

- containing light species: a multi-method approach, *Thin Solid Films* 686 (2019), 137416, <https://doi.org/10.1016/j.tsf.2019.137416>.
- [16] K. Arstila, J. Julin, M.I. Laitinen, J. Aalto, T. Konu, S. Kärkkäinen, S. Rahkonen, M. Raunio, J. Iitonen, J.-P. Santanen, T. Tuovinen, T. Sajavaara, Potku – new analysis software for heavy ion elastic recoil detection analysis, *Nucl. Instrum. Methods Phys. Res. Sect. B Beam Interact. Mater. At.* 331 (2014) 34–41, <https://doi.org/10.1016/j.nimb.2014.02.016>.
- [17] M.B. Kalinowski, C. Pistner, Isotopic signature of atmospheric xenon released from light water reactors, *J. Environ. Radioact.* 88 (2006) 215–235, <https://doi.org/10.1016/j.jenvrad.2006.02.003>.
- [18] J. Rest, M.W.D. Cooper, J. Spino, J.A. Turnbull, P. Van Uffelen, C.T. Walker, Fission gas release from UO₂ nuclear fuel: a review, *J. Nucl. Mater.* 513 (2019) 310–345, <https://doi.org/10.1016/j.jnucmat.2018.08.019>.
- [19] H.O. Pierson, *Handbook of Refractory Carbides & Nitrides: Properties, Characteristics, Processing and Applications*, William Andrew, 1996.
- [20] B. Song, Y. Li, Z. Cong, Y. Li, Z. Song, J. Chen, Effects of deposition temperature on the nanomechanical properties of refractory high entropy TaNbHfZr films, *J. Alloys Compd.* 797 (2019) 1025–1030, doi:10.ghx5t6.
- [21] F. Cemin, S.R.S. de Mello, C.A. Figueroa, F. Alvarez, Influence of substrate bias and temperature on the crystallization of metallic NbTaTiVZr high-entropy alloy thin films, *Surf. Coat. Technol.* 421 (2021), 127357, <https://doi.org/10.1016/j.surfcoat.2021.127357>.
- [22] S.Y. Chen, Y. Tong, K.-K. Tseng, J.-W. Yeh, J.D. Poplawsky, J.G. Wen, M.C. Gao, G. Kim, W. Chen, Y. Ren, R. Feng, W.D. Li, P.K. Liaw, Phase transformations of HfNbTaTiZr high-entropy alloy at intermediate temperatures, *Scr. Mater.* 158 (2019) 50–56, <https://doi.org/10.1016/j.scriptamat.2018.08.032>.
- [23] N. Tütün, D. Canadinc, A. Motallebzadeh, B. Bal, Microstructure and tribological properties of TiTaHfNbZr high entropy alloy coatings deposited on Ti6Al4V substrates, *Intermetallics* 105 (2019) 99–106, doi:10.ggd47q.
- [24] D. Kaoumi, A.T. Motta, R.C. Birtcher, A thermal spike model of grain growth under irradiation, *J. Appl. Phys.* 104 (2008), 073525, <https://doi.org/10.1063/1.2988142>.
- [25] Y. Zhang, W. Jiang, C. Wang, F. Namavar, P.D. Edmondson, Z. Zhu, F. Gao, J. Lian, W.J. Weber, Grain growth and phase stability of nanocrystalline cubic zirconia under ion irradiation, *Phys. Rev. B* 82 (2010), 184105, <https://doi.org/10.1103/PhysRevB.82.184105>.
- [26] Y. Zhang, C. Silva, T.G. Lach, M.A. Tunes, Y. Zhou, L. Nuckols, W.L. Boldman, P. D. Rack, S.E. Donnelly, L. Jiang, L. Wang, W.J. Weber, Role of electronic energy loss on defect production and interface stability: comparison between ceramic materials and high-entropy alloys, *Curr. Opin. Solid State Mater. Sci.* 26 (2022), 101001, <https://doi.org/10.1016/j.cossms.2022.101001>.
- [27] C.P. Race, D.R. Mason, M.W. Finnis, W.M.C. Foulkes, A.P. Horsfield, A.P. Sutton, The treatment of electronic excitations in atomistic models of radiation damage in metals, *Rep. Prog. Phys.* 73 (2010), 116501, <https://doi.org/10.1088/0034-4885/73/11/116501>.
- [28] C. Stodel, M. Toulemonde, C. Fransen, B. Jacquot, E. Clément, G. Frémont, M. Michel, C. Dufour, “Thermal Spike” model applied to thin targets irradiated with swift heavy ion beams at few MeV/u, *EPJ Web Conf.* 229 (2020) 05001, <https://doi.org/10.1051/epjconf/202022905001>.
- [29] M. Toulemonde, W.J. Weber, G. Li, V. Shutthanandan, P. Kluth, T. Yang, Y. Wang, Y. Zhang, Synergy of nuclear and electronic energy losses in ion-irradiation processes: the case of vitreous silicon dioxide, *Phys. Rev. B* 83 (2011), 054106, <https://doi.org/10.1103/PhysRevB.83.054106>.
- [30] R.E. Stoller, M.B. Toloczko, G.S. Was, A.G. Certain, S. Dwaraknath, F.A. Garner, On the use of SRIM for computing radiation damage exposure, *Nucl. Instrum. Methods Phys. Res. Sect. B Beam Interact. Mater. At.* 310 (2013) 75–80, <https://doi.org/10.1016/j.nimb.2013.05.008>.
- [31] J.C. Liu, J. Li, J.W. Mayer, Temperature effect on ion-irradiation-induced grain growth in Cu thin films, *J. Appl. Phys.* 67 (1990) 2354–2358, <https://doi.org/10.1063/1.345530>.
- [32] D.E. Alexander, G.S. Was, L.E. Rehn, Ion-induced grain growth in multilayer and coevaporated metal alloy thin films, *Nucl. Instrum. Methods Phys. Res. Sect. B Beam Interact. Mater. At.* 59–60 (1991) 462–466, [https://doi.org/10.1016/0168-583X\(91\)95260-K](https://doi.org/10.1016/0168-583X(91)95260-K).
- [33] D.E. Alexander, G.S. Was, Thermal-spike treatment of ion-induced grain growth: theory and experimental comparison, *Phys. Rev. B* 47 (1993) 2983–2994, <https://doi.org/10.1103/PhysRevB.47.2983>.
- [34] Y.-Q. Chang, Q. Guo, J. Zhang, L. Chen, Y. Long, F.-R. Wan, Irradiation effects on nanocrystalline materials, *Front. Mater. Sci.* 7 (2013) 143–155, <https://doi.org/10.1007/s11706-013-0199-3>.
- [35] K. Trachenko, J.M. Pruneda, E. Artacho, M.T. Dove, How the nature of the chemical bond governs resistance to amorphization by radiation damage, *Phys. Rev. B* 71 (2005), 184104, <https://doi.org/10.1103/PhysRevB.71.184104>.
- [36] K. Trachenko, Understanding resistance to amorphization by radiation damage, *J. Phys. Condens. Matter* 16 (2004) R1491–R1515, <https://doi.org/10.1088/0953-8984/16/49/R03>.
- [37] R. Shu, D. Lundin, B. Xin, M.A. Sortica, D. Primetzhofer, M. Magnuson, A. le Febvrier, P. Eklund, Influence of metal substitution and ion energy on microstructure evolution of high-entropy nitride (TiZrTaMe)N_{1-x} (Me = Hf, Nb, Mo, or Cr) films, *ACS Appl. Electron. Mater.* 3 (2021) 2748–2756, <https://doi.org/10.1021/acsaem.1c00311>.
- [38] E. Lewin, Multi-component and high-entropy nitride coatings—a promising field in need of a novel approach, *J. Appl. Phys.* 127 (2020), 160901, <https://doi.org/10.1063/1.5144154>.
- [39] Y. Zhang, S. Zhao, W.J. Weber, K. Nordlund, F. Granberg, F. Djurabekova, Atomic-level heterogeneity and defect dynamics in concentrated solid-solution alloys, *Curr. Opin. Solid State Mater. Sci.* 21 (2017) 221–237, <https://doi.org/10.1016/j.cossms.2017.02.002>.
- [40] F. Körmann, Y. Ikeda, B. Grabowski, M.H.F. Sluiter, Phonon broadening in high entropy alloys, *Npj Comput. Mater.* 3 (2017) 1–9, <https://doi.org/10.1038/s41524-017-0037-8>.
- [41] Z. Su, T. Shi, J. Yang, H. Shen, Z. Li, S. Wang, G. Ran, C. Lu, The effect of interstitial carbon atoms on defect evolution in high entropy alloys under helium irradiation, *Acta Mater.* 233 (2022), 117955, <https://doi.org/10.1016/j.actamat.2022.117955>.